

# Picometer differential wavefront metrology by nonlinear Zernike wavefront sensing for LUVOIR

Dustin B. Moore\* and David C. Redding  
Jet Propulsion Laboratory, California Institute of Technology,  
4800 Oak Grove Drive, Pasadena CA 91109

## ABSTRACT

We propose the Nonlinear Zernike wavefront sensor (NLZWFS) for out-of-band differential wavefront sensing to augment primary mirror stability on LUVOIR and similar mission concepts during exoplanet coronagraphy. This new data analysis paradigm involving a full polychromatic scalar physical optics model for the phase-shifting Zernike wavefront sensor removes the linearity assumptions which would otherwise prevent accurate sensing. We show Monte-Carlo simulations of NLZWFS and focus-diverse phase retrieval to understand the exposure times necessary to achieve picometer-level stability in the telescope wavefront.

**Keywords:** optical metrology, wavefront sensing, Zernike wavefront sensor, phase retrieval

## 1. INTRODUCTION

NASA chartered a study of a potential Large Ultraviolet-Optical-Infrared space telescope mission (LUVOIR), to survey nearby solar systems to discover and characterize exoplanets. The ultimate objective is to discover and characterize candidate Earth-like rocky planets (exo-Earths) in the Habitable Zones (HZ) of Sun-like stars. One realization of LUVOIR under consideration would use a coronagraph optical instrument for high-contrast direct imaging and spectroscopy of potential exo-Earths. Coronagraphs block the on-axis light from a target star while passing the much dimmer light reflected from planets orbiting the star. With repeated direct-imaging of hundreds of target stars, LUVOIR would record the positions of many exoplanets and, over time, allow estimation of their orbital parameters. Spectroscopic observations of exoplanets in the HZ would characterize their atmospheres and look for the chemical signatures of possible life: water, oxygen, ozone, carbon dioxide and methane. The LUVOIR mission would be a powerful general astrophysics observatory with diffraction-limited imaging and high-resolution spectroscopy covering the far-ultraviolet through the near-infrared.

In the classic-Lyot style coronagraph mode, exoplanet imaging is accomplished by focusing light captured by the telescope onto an occulting mask as illustrated in Figure 1. The mask blocks the light at the very center of the field but passes light from exoplanets a very small angle off-center. After this mask, the beam is re-collimated and passed through a Lyot pupil stop removing target starlight diffracted by the occulting mask. Finally, the beam is re-focused to form a starlight-suppressed image of the exoplanetary system. This image can be produced either directly on a detector for broadband imaging or on a lenslet array at the entrance of an integral field spectrograph for wavelength-resolved imaging.

The coronagraphs currently planned for LUVOIR are evolved versions of the Lyot design with two operating modes. The Apodized Pupil Lyot Coronagraph<sup>1,2</sup> (APLC) mode and the Apodized Vector Vortex Coronagraph<sup>3</sup> (AVVC) mode add an apodizer at a pupil before the coronagraph mask to introduce diffracting features that direct the on-axis light more completely into the mask and Lyot stop. The AVVC uses a vector vortex phase mask to suppress the on-axis light rather than an apodizing mask. LUVOIR includes both modes in its coronagraph by using multiple filter wheels to change configuration. The two different modes have complementary capabilities; the APPLC is more tolerant of tip-tilt aberrations and resolved stellar objects but it has a larger inner working angle than the AVVC. Together, the modes would permit LUVOIR to do closer-in observations with the AVVC when the star is nearly unresolved and more robust observations with the APPLC for closer, hence apparently larger, stars.

---

\*dustin.moore@jpl.nasa.gov

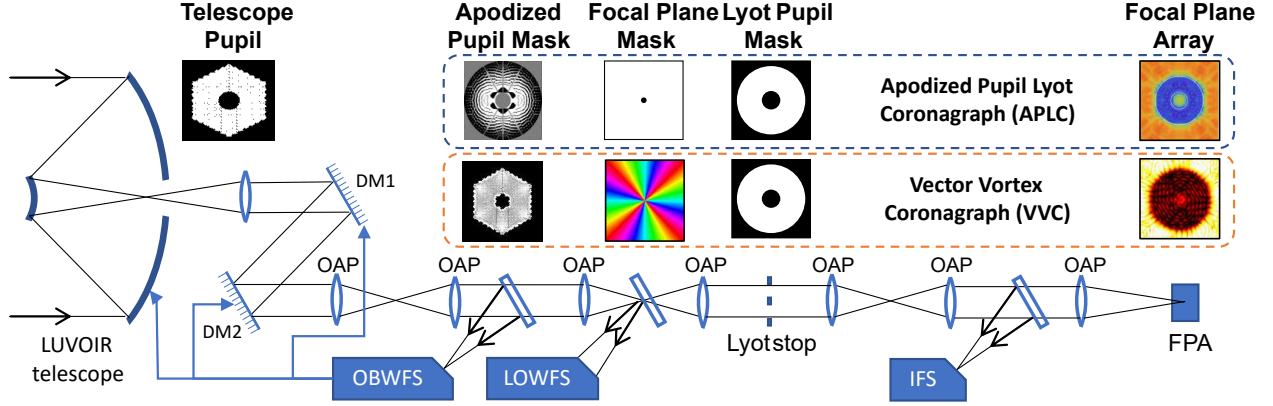


Figure 1. Potential LUVUOIR coronagraph elements including hardware for the APLC and VVC modes. The telescope is pointed at a target star, whose light is passed to the coronagraph, through an apodized pupil mask, and then focused on a focal plane mask. The mask suppresses the target star image. The rest of the light, including the off-axis planet light, passes by the mask. Downstream, a Lyot stop suppresses residual diffracted starlight, and then the planet light is refocused onto a Focal Plane Array (FPA) detector, or fed into an Integral Field Spectrograph. Two Deformable Mirrors (DMs) are used to establish high contrast. OBWFS and LOWFS wavefront sensors (see Sections 2, 3) drive the DMs and primary mirror segments to stabilize wavefront and intensity variations to preserve contrast.

## 2. CONCURRENT OUT OF BAND WAVEFRONT SENSING

Coronagraphs require careful shaping of the complex amplitude field using Deformable Mirrors (DMs) prior to the masks. With one DM at a pupil image and another at a different location, both phase and amplitude aberrations can be addressed. Iterative algorithms such as electric field conjugation (EFC) then act to suppress speckles of light that occur in the “dark hole” detection region on the focal plane. Successive iterations of such algorithms measure speckles on the FPA and then adjust the DMs to suppress speckle in the dark hole region. This establishes the contrast, the ratio of peak starlight to peak planet light, required to image exoplanets. The contrast required to direct image exo-Earths orbiting Sun-like stars is  $10^{-11}$ . Achieving this contrast requires shaping of the wavefront error or optical path differences over the pupil to a precision of about 20 pm RMS. Note that this is not a requirement for nulling or fully-correcting the wavefront error, just precise control. Furthermore, the wavefront shape once established by the DMs, must be preserved with an accuracy of 10 pm RMS at the highest spatial frequencies. This includes stabilizing drift effects from throughout the beam train, from the large telescope, the relay optics, and the DMs themselves.<sup>4</sup> This “ultra-stability” cannot be provided by purely passive means since basic material drifts quickly overwhelm the extraordinarily tight precision required. Therefore, active means, including a wavefront sensing method operating concurrently with the science instrument, will be required to preserve the speckle nulling during coronagraphy.

For this paper, we consider concurrent wavefront sensing (WFS) strategies for an Out-Of-Band Wavefront Sensing (OBWFS) method that would acquire a copy of the post-DM field at a wavelength shorter than the science instrument. As sketched in Figure 1, the OBWFS would sample a pupil-like beam post DMs using a dichroic mirror. This would be done for several reasons; the first being that sampling the post DM fields eliminates most sources of drift (significantly that of the DMs) that other metrology methods, such as edge sensors on the primary mirror, might miss due to non-common paths. The second reason is efficiency; since exoplanets have most of their power in the longer wavelengths, OBWFS decreases the amount of exoplanet light that would be wasted for WFS purposes rather than being passed to the science camera. The third reason is accuracy as the shorter wavelengths are inherently more useful for wavefront sensing of tiny optical path differences than the longer wavelengths going to the science camera. A final reason is spatial resolution: since OBWFS would sample the entire post-DM pupil it has the advantage of accessing all spatial frequencies in the field. This is in contrast to concurrent WFS strategies like the Low Order Wavefront Sensor<sup>5</sup> (LOWFS) which have an integral spatial filter that prevents recovery of fine wavefront detail.

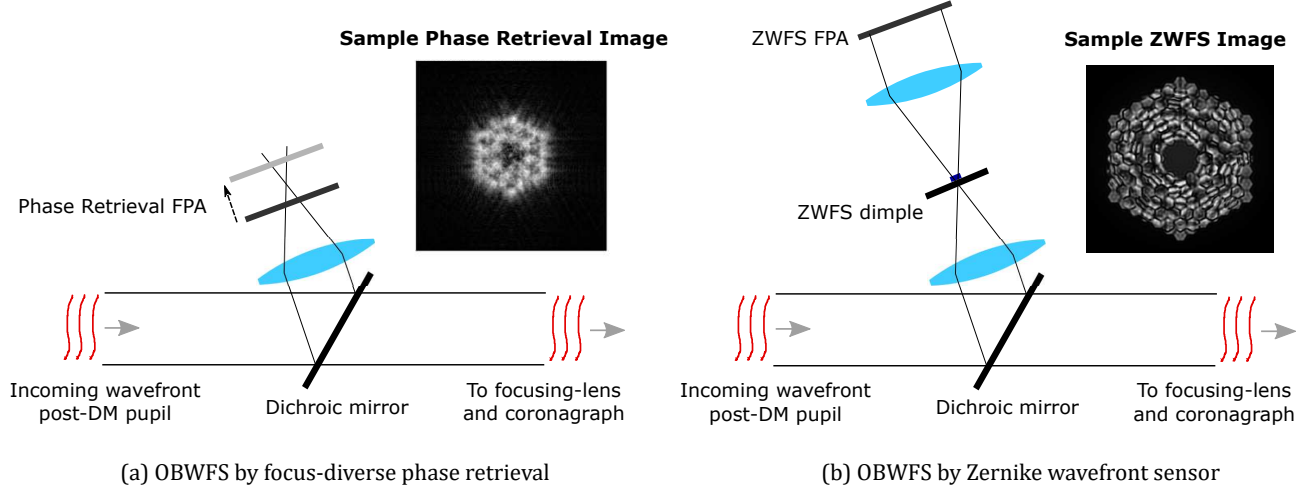


Figure 2. Sketches of optical layouts and sample output images for OBWFS strategies such as (a) focus-diverse phase retrieval (FDPR) and (b) Zernike wavefront sensing (ZWFS). If FDPR, the FPA is on a stage that allows it to move through focus. For ZWFS, the ZWFS dimple is on a stage moving transverse to the beam that allows introduction of various dimples into the beam.

### 3. PHASE RETRIEVAL AND LINEARIZED ZERNIKE STRATEGIES FOR OBWFS

We consider two different high-precision image-based wavefront sensing strategies for OBWFS that require little additional hardware and leave few opportunities for additional non-common path errors and calibration issues.

The first strategy uses focus-diverse phase retrieval<sup>6–9</sup> (FDPR) applied to OBWFS illustrated in Figure 2 (a). FDPR has an established history for fine WFS of space telescopes including Hubble<sup>10,11</sup> and the James Webb Space Telescope.<sup>8,12</sup> In the FDPR strategy, light from the post-DM pupil is picked off and focused by a lens or mirror to a FPA that is near focus. The FPA then acquires what is usually two or more Point Spread Function (PSF) images at various offsets relative to perfect focus. This ensemble of images forms the data for a phase retrieval algorithm such as modified versions<sup>8,9</sup> of the venerable Gerchberg-Saxton algorithm<sup>13</sup> or similar iterative-transform algorithms like the HIO algorithm.<sup>14</sup> For this work, though, we utilize the FDPR algorithm form<sup>6,7</sup> that matches a parametric model for the FPA output to the measured data by minimizing a data consistency metric such as the sum of the squared errors between data and a parametric model. The model includes free parameters for the unknowns in the system that affect phase of the pupil-like field incident on the OBWFS. We will refer to the data consistency metric as an error metric as it will be the squared error between measured data and model prediction. The error metric is reduced by a gradient-descent nonlinear optimization like the Broyden-Fletcher-Goldfarb-Shanno<sup>15</sup> (BFGS) algorithm that iteratively adjusts free parameters until a minimum of the error metric is located. For this work, the BFGS algorithm was provided a computationally fast function generating the gradient of the metric with respect to the free parameters. The gradient function was found by means of reverse mode of algorithmic differentiation<sup>16</sup> (RMAD) which greatly simplifies development of such gradients for phase-retrieval like problems.

The second OBWFS strategy we consider uses the Zernike wavefront sensor<sup>17–20</sup> (ZWFS) hardware shown in Figure 2 (b). This WFS is essentially the classic phase-contrast method of Zernike<sup>21</sup> that is most often applied to phase microscopy applications but used here to infer quantitative pupil phase aberration. For ZWFS, light is focused as in FDPR but at focus there is a transparency with a small circular feature that produces a  $\pi/2$  radian phase delay centered on the point spread function. This feature, called the dimple, is on the order of a Rayleigh criterion<sup>22</sup> in diameter and it delays the central core of the PSF to yield a reference spherical beam to which the rest of the field can be compared. The ZWFS is a common-mode and self-referencing analog of a Mach-Zehnder interferometer<sup>18</sup> where phase aberrations in the input yield phase-sensitive intensity variations in the collimated space after the PSF plane. Images are collected with dimples having various central phase delays to collect an

ensemble of images for the ZWFS algorithm to analyze. Typical useful values for dimples correspond to optical phase delays of  $\pi$ ,  $\pi/2$ , 0 and  $-\pi/2$  radians.

Systems using ZWFS have been demonstrated on-sky for ground telescope wavefront sensing applications.<sup>23–26</sup> A variation on the classic ZWFS design is the LOWFS being considered for the WFIRST mission concept and being demonstrated on a high fidelity testbed.<sup>5</sup> As sketched in Figure 1, the LOWFS sensor integrates a ZWFS dimple into the Lyot focal plane mask. Normally, a Lyot focal plane mask would absorb the target star light but in LOWFS the Lyot focal plane obscuration is reflective and has with a small phase dimple. Light reflecting off the focal plane mask can then be collimated and used for sensing the lower order Zernike modes. The higher spatial frequency modes are filtered out due to the relatively narrow extent of the Lyot focal plane obscuration.

The prior ZWFS implementations we are aware of utilize an approximation that is more valid when the overall wavefront error magnitude is small compared to a wave. When this is true, there are simple approximate expressions for the wavefront phase that are linear in measured FPA intensity like Eq. (11) in Wallace<sup>19</sup> and Eq. (8-3) in Goodman.<sup>22</sup> For simplicity, we refer to these prior ZWFS reconstruction algorithms that use significant approximations as linearized-ZWFS methods. This linearization is convenient but it reduces the accuracy of the retrieved phase when the wavefront aberrations differs significantly from perfectly nulled. For the hypothetical LUVOIR coronagraph, it is expected that the post-DM wavefront will be some complicated wavefront solution that the speckle nulling algorithm has settled upon over many iterations and thus linearized-ZWFS algorithms will be insufficiently accurate. Some of these effects can be mitigated by including second-order effects as in N'Diaye<sup>20</sup> to demonstrate nanometer-accurate results<sup>26</sup> on-sky. However, for picometer-accurate OBWFS, the approximate methods are insufficiently accurate.

#### 4. NONLINEAR ZERNIKE WAVEFRONT SENSOR

We developed a new ZWFS data processing method to yield what we term the Nonlinear Zernike wavefront sensor (NLZWFS) which alleviates the accuracy issues associated with linearized-ZWFS. Like the FDPR method chosen in Section 3, NZWFS fits a parameterized model to the observed data by minimizing an error metric. NZWFS uses polychromatic scalar Fourier optics to propagate fields from the telescope pupil to the plane of the measured data FPA. Assuming a useful minimum of the error metric can be found where the parameterized model closely matches the measured data, NZWFS is not subject to gross nonlinearity errors or biases due to the broadband nature of the light used.

Explanation of the ‘forward’ model for NLZWFS begins with discretized model for the phase in the pupil-like plane entering the OBWFS represented by a two-dimensional array. Assume that the optical path differences can be decomposed into some ensemble of  $J$  not-necessarily orthogonal two-dimensional basis functions  $\mathbf{Z}_j$ . Let the optical path difference in the post-DM field at a particular reference wavelength  $\lambda_o$  be denoted in radians by an array

$$\Phi = \sum_{j=1}^J a_j \mathbf{Z}_j, \quad (1)$$

where  $a_j$  is a coefficient describing the component of the wavefront aberration due to the  $j$ th basis function. The algorithm we propose uses an explicitly polychromatic model where  $L$  discrete wavelength-dependent irradiance contributions will be summed to estimate the FPA detected irradiance. For convenience, define  $\Lambda_l = \lambda_o/\lambda_l$  where  $\lambda_l$  is the wavelength of the  $l$ th discrete irradiance contribution.

A model for a discretely sampled equivalent of the post-DM field is the complex-valued array

$$\mathbf{g} = \mathbf{A} \circ \exp(i\Lambda_l \Phi), \quad (2)$$

where the array  $\mathbf{A}$  is an estimate for the post-DM pupil amplitude that has been thresholded at zero to be non-negative and the  $\circ$  operator indicates element-wise multiplication between two like-sized array quantities.

For simplicity, we assume the post-DM pupil coming into the OBWFS is in the front focal plane of the first lens of the sensor and that the plane containing the transparency with the dimple is in the back focal plane of the first lens. Consequently, the field in the back focal plane and incident on the transparency can be described

using a single Fourier transform such as Eq. (5-19) in Goodman<sup>22</sup> under suitable approximations. For fast approximation of such continuous Fourier transforms using discrete arrays there is the chirp-Z transform<sup>27</sup> and matrix-multiply.<sup>28</sup> These two realizations of a Discrete Fourier Transform (DFT) are useful for gradient-based polychromatic phase-retrieval since they get around some of the performance and sampling limitations imposed by the well known fast Fourier transform. For NLZWFS, we use the matrix-multiply operation represented by Eq. (15) in Moore<sup>28</sup> and denote the propagation of the array  $\mathbf{g}$  to an array  $\mathbf{h}$  using an operation  $\mathcal{F}(\mathbf{g}, \alpha)$ .  $\alpha$  is unit-less scaling term that is a property of the physical optics system simulation that often must be fit to the measured data for accurate modeling. In more physical and dimensioned terms,

$$\alpha = \frac{\Delta_{\mathbf{h}} \Delta_{\mathbf{g}}}{z \lambda_o} \quad (3)$$

where  $z$  is the lens back-focal length and  $\Delta_{\mathbf{h}}$  and  $\Delta_{\mathbf{g}}$  are the distances between samples in  $\mathbf{h}$  and  $\mathbf{g}$ , respectively.

The field just-prior to the dimple transparency for a wavelength  $l$  is

$$\mathbf{h} = \Lambda_l \mathcal{F}(\mathbf{g}, \Lambda_l \alpha_o), \quad (4)$$

where  $\alpha_o$  is the  $\alpha$  for the propagation at the reference wavelength  $\lambda_o$ . The initial scaling factor of  $\Lambda_l$  in Eq. (4) preserves the power conservation as a function of wavelength given the DFTs defined in the earlier works.<sup>27,28</sup> The later  $\Lambda_l \alpha_o$  term in Eq. (4) accommodates the wavelength-dependent scaling in the DFT relative to the nominal condition of  $\alpha_o$  corresponding to  $\lambda = \lambda_o$ .

Let the real-valued array  $\mathbf{D}_k$  be a radian-denominated optical path length difference due to the ZWFS phase dimple in the  $k$ th acquired image and  $\mathbf{S}$  be an array representing the amplitude associated with any field-stop imposed in the dimple plane. In the thin-object approximation, the field just after the dimple plane is then

$$\mathbf{H}_k = \mathbf{S} \circ \exp(i \Lambda_l \mathbf{D}_k) \circ \mathbf{h}. \quad (5)$$

Note: the size of the arrays contributing to  $\mathbf{g}$  must be large enough and well-sampled enough that there are numerous samples (e.g. 8 to 24) across the diameter of the dimple feature in  $\mathbf{D}_k$ .

Assuming that the dimple transparency is in the front-focal plane of the second lens and that the FPA is situated at the back-focal plane of the second lens, the irradiance falling on the detector for a given image  $k$  and at wavelength sample  $l$  is

$$\mathbf{I}_{k,l} = s_l |\Lambda_l \mathcal{F}(\mathbf{H}_k, \Lambda_l \alpha_o)|^2, \quad (6)$$

where  $s_l$  is a spectral weighting value for the  $l$ th wavelength. Since Eqs. 4 and 6 share the same value of  $\Lambda_l \alpha_o$ , it has been implicitly assumed that the ratio of the sampling interval in  $\mathbf{g}$  to the focal length of the first lens is the same as the ratio of the sampling interval of the FPA to the focal length of the second lens.

The total irradiance detected in the  $k$ th ZWFS image due to all of the discretely sampled per-wavelength irradiances is

$$\mathbf{I}_k = \sum_{l=1}^L \mathbf{I}_{k,l}, \quad (7)$$

where the summations is assumed to be element-wise over the samples of realizations of  $\mathbf{I}_{k,l}$ .

As in Moore,<sup>28</sup> a model for the FPA detected irradiance given  $\mathbf{I}_k$ , including a detector gain  $\beta_k$  and detector bias  $\gamma_k$ , is

$$\mathbf{M}_k = \beta_k \mathbf{I}_k + \gamma_k \mathbf{1}, \quad (8)$$

where  $\mathbf{1}$  is an array of values which are all 1. Define  $\mathbf{D}_k$  to be the  $k$ th measured ZWFS data from the FPA and let  $w_k$  be a array of weightings on samples in the FPA coordinates to be described below. A weighted sum-of-squared error metric between the model and measured data for the  $k$ th ZWFS data is

$$E_k = \sum_{x \in X} w_k[x] \circ (\mathbf{M}_k[x] - \mathbf{D}_k[x])^2, \quad (9)$$

where the summation is taken over the set of pixels  $X$  in the array linearly indexed by  $x$ . The unknown  $\beta_k$  and  $\gamma_k$  can be computed using Appendix C of Moore<sup>28</sup> to make Eq. 9 and detector gain-and-bias invariant metric.<sup>29</sup> Summing over the  $E_k$  for individual data collections yields a single scalar

$$E = \sum_{k=1}^K E_k, \quad (10)$$

a sum-of-squared error metric for the  $K$  arrays of measured ZWFS data. We define samples of the array  $w_k$  to take the value zero where the FPA has unreliable pixels and a value of  $\mathbf{D}^{-1}$  (element-wise inverse) everywhere else. This causes Eq. (10) to be approximately proportional to the negative log-likelihood function for a Poisson random process yielding  $\mathbf{D}_k$  given the parameters of  $\mathbf{I}_k$  assuming that  $\mathbf{D}_k$  is a good approximation for the variance of  $\mathbf{I}_k$  and that the photon flux is large enough that the Poisson distribution can be approximated with a Gaussian.

A computer algorithm that computes  $\nabla E$  with respect to the  $a_j$  and the values other potential nuisance parameters like  $\alpha_o$  and the pixels in  $\mathbf{A}$  can be programmed using the RMAD results in earlier literature.<sup>16,28</sup> It is even possible to compute gradients with respect to unknowns in the dimple transparency domain should  $\mathbf{D}_k$  or  $\mathbf{S}$  be unknown. To date we have only explored solving for unknown  $a_j$  and  $\alpha_o$  using gradient-based optimization and these other unknowns terms have been estimated by trial and error.

Phase estimation in the NLWFS method proceeds as follows,

1. Data  $\mathbf{D}_k$  is acquired for various dimples having various delays.
2. Approximate starting values for  $a_j$  and any other terms that are to be found by optimization are input into the algorithm.
3. The BFGS algorithm is applied to minimize  $E$  by iterative evaluation of  $E$  and  $\nabla E$  with respect to the unknown  $a_j$  and any other unknown terms.

If a robust minimum is found and  $\mathbf{I}_k$  matches  $\mathbf{D}_k$  well, the final value of  $a_j$  used by the BFGS algorithm is consistent with a maximum likelihood estimation of  $a_j$  given  $\mathbf{D}_k$ . In some cases, a robust minimum may not be found without multiple iterations on Step 3 where different types of unknowns are allowed to vary. For instance, if  $\mathbf{Z}_j$  are Zernike functions on a nearly-filled pupil, it may improve the probability of success to optimize for just the coefficients of the lowest-order functions first before allowing the higher order terms and  $\alpha_o$  vary.

## 5. MONTE-CARLO SIMULATION

To demonstrate OBWFS using FDPR and NLZWFS, we applied them in a Monte-Carlo simulation experiment to compute segment piston, tip and tilt for a LUVOIR-like segmented aperture telescope having 120 segments. This Monte-Carlo experiment assessed how well a change in wavefront on the order of 10 pm RMS between two epochs in time could be sensed in the presense of a larger fixed error having departures from null of 41 nm RMS on average. An example wavefront error for an initial epoch is shown in Figure 3 (a) and an example change from initial epoch to final epoch is shown in Figure 3 (b). For the Monte-Carlo simulation, the fixed aberrations and the change aberrations were randomly generated.

The simulated light used was  $\lambda_o = 440$  nm and had a uniformly-distributed 22.3% spectral bandwidth approximating the B waveband. This is realistic given the OBWFS envisioned for LUVOIR. Photon counting noise (Poisson-distributed) was applied to the simulated data for various fluxes on the interval between  $2 \times 10^9$  and  $2 \times 10^{13}$  photons per time epoch. Read noise, flat-fielding and other error sources involving calibration were neglected to understand the essential photon efficiency limits of WFS.

The NLZWFS data simulated for each epoch included images for dimples having delays of  $+\pi/2$  and  $-\pi/2$  radians of phase. An example image in the initial case is shown in Figure 3 (c). After accounting for the mirroring of both coordinate axes about the origin due the beam being relayed through two positive lenses, it is readily seen that there is a correlation between this simulated ZWFS image in Figure 3 (c) and the large initial

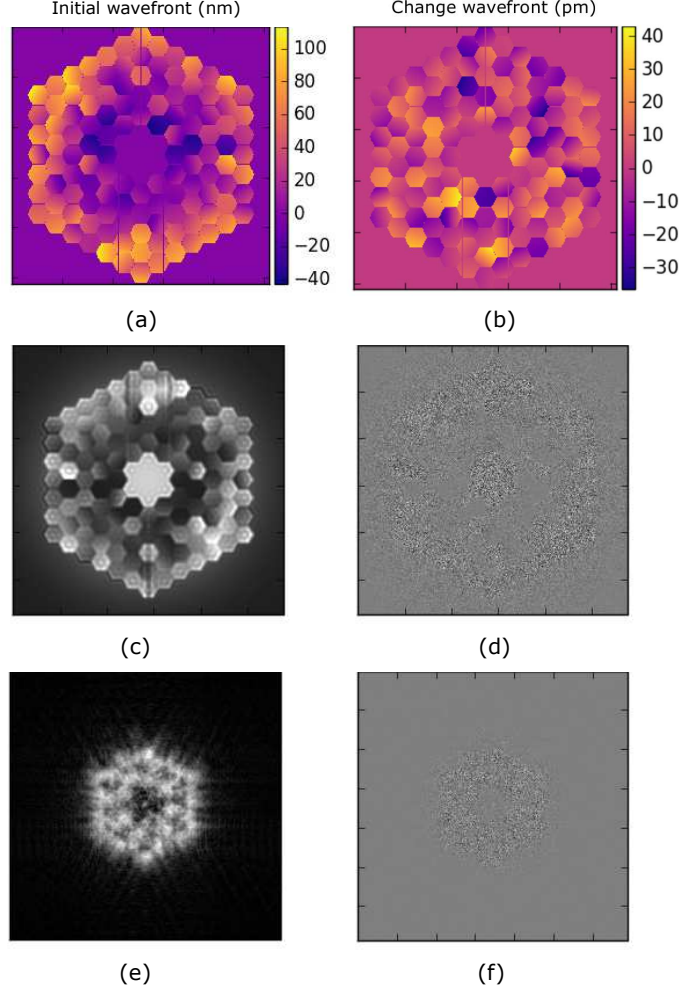


Figure 3. (a) Example initial epoch randomly-generated wavefront, (b) example change from initial epoch’s wavefront to final epoch’s wavefront, (c) Example simulated ZWFS data image having  $2 \times 10^{10}$  photons, (d) Example difference between ZWFS image at initial epoch and final epoch, (e) Example FDPR PSF data image having  $2 \times 10^{10}$  photons and (f) Example difference between FDPR PSF at initial epoch and final epoch.

wavefront phase shown in Figure 3 (a). The high-degree of spatial correlation between wavefront phase and image intensity illustrates the principal signal exploited by all ZWFS algorithms. However, as shown in Figure 3 (c), the true ZWFS images have “ringing” in the intensity near segment boundaries. The linearized-ZWFS algorithms and even the second order methods like N’Diaye<sup>20</sup> do not account for this artifact of the physical optics phenomenon.

The first-order correlation between wavefront and ZWFS image observed above repeats in the differences in wavefront and observed intensity between the first and final epochs. Though difficult to observe due to photon noise, the change in wavefront from Figure 3 (b) approximately maps to the difference between the ZWFS images in the final and initial epochs shown in Figure 3 (d).

The FDPR PSF data simulated for each epoch included two frames: one with a defocus of 3 waves peak-to-valley and the other with a defocus of  $-3$  waves peak-to-valley. An example initial epoch FDPR PSF is shown in Figure 3 (e) and the difference between a final epoch PSF and an initial epoch PSF in Figure 3 (f). Unlike ZWFS modes, the relationship between observed data and the underlying PSF is highly nonlinear and spatially uncorrelated; there is no easy comparison between Figures 3 (a)-(b) and Figures 3 (e)-(f).

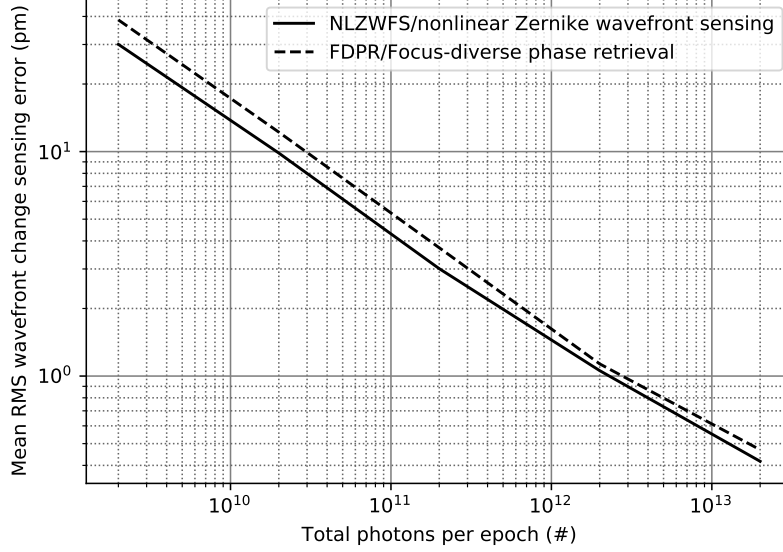


Figure 4. Plot showing the mean RMS of the wavefront sensing error (evaluated over the ensemble of Monte-Carlo experiments) for various photon fluxes.

Finally, to ensure that the Monte-Carlo simulation was evaluating the small change detection capabilities of the algorithms rather than their stagnation properties or “capture range,” a randomized starting phase estimate for each optimization was provided to the algorithm that was within about 4 nm RMS of the true initial wavefront. This is equivalent to presuming an estimate for the wavefront is available prior to engaging concurrent OBWFS. We envision such estimates might be obtained using FDPR using many focus planes or through some other WFS method like a Shack-Hartman detector.

### 5.1 Simulation Results

The simulation results are described in Figure 4 in terms of the mean wavefront sensing error as a function of photon flux. The NLZWFS wavefront sensing method shows a consistent, if slight, photon efficiency advantage. With less than  $10^{12}$  photons per epoch, NLZWFS wavefront sensing error was about 20% better and above that threshold NLZWFS’s error was about 9% better.

Stark<sup>30</sup> assembled a list of target stars for an exoplanet evaluation study using the notional LUVOIR coronagraph. Most of these stars have a stellar magnitude in the B waveband of  $m_B = 6$  with some target stars being as dim as stellar magnitude  $m_B = 10$ . Assuming a clear aperture of 135 meters-squared, perfect transmittance of the telescope and perfect efficiency of detection, the exposure durations on a  $m_B = 6$  target star necessary for collecting data for each epoch are listed in Table 1. The same but for a  $m_B = 10$  star is shown in Table 2. Note that this analysis does not account for calibration errors, losses in the optical system, detector efficiency or read noise.

Table 1. Expected exposure times for a target star with a B stellar magnitude of  $m_B = 6$ .

Exposure time per epoch to achieve	FDPR	NLZWFS
10 pm RMS change error	3.6 seconds	2.4 seconds
5 pm RMS change error	13.4 seconds	9.0 seconds
1 pm RMS change error	382 seconds	272 seconds



Table 2. Expected exposure times for a target star with  $m_B = 10$ .

Exposure time per epoch to achieve	FDPR	NLZWFS
10 pm RMS change error	142 seconds	93 seconds
5 pm RMS change error	532 seconds	358 seconds
1 pm RMS change error	3.6 hours	3.0 hours

## 6. SUMMARY

Direct imaging of extrasolar planets using a coronagraph will require extraordinarily stable total system wavefronts (to the picometer level) in order to preserve coronagraph contrast at the  $10^{-11}$  level. The methods described here for wavefront sensing concurrent with coronagraph observations provide the measurements needed to accomplish this.

We introduced the nonlinear Zernike wavefront sensing algorithm which allows for high-accuracy wavefront sensing in the presence of non-null wavefronts. It incorporates a full polychromatic broadband solution to the Zernike wavefront sensing data processing. This new wavefront sensing mode was compared to focus-diverse phase retrieval and their performance as a function of target star brightness was evaluated. We showed wavefront sensing times commensurate with wavefront drift time constants for most stars in the current LUVOIR target list given assumptions of perfect telescope efficiency, optimal detectors and no calibration errors. The new Nonlinear Zernike Wavefront Sensor approach always showed the best performance, but focus-diverse phase retrieval was close behind.

Work is underway to demonstrate the methods described here in simple laboratory testbeds. These initial tests will be in air which will limit ultimate performance. In the longer term, demonstration in vacuum will be required so we are pursuing implementation as part of the Decadal Survey Testbed<sup>31</sup> which will include coronagraph and WFS instruments.

## ACKNOWLEDGMENTS

We would like to thank J. K. Wallace, K. Jackson, S. Zareh and J. Steeves of JPL for enlightening discussions.

The information presented about the LUVOIR mission concept is pre-decisional and is provided for planning and discussion purposes only. This research was conducted at the Jet Propulsion Laboratory, California Institute of Technology. Government sponsorship is acknowledged.

## REFERENCES

- [1] N'Diaye, M., Soummer, R., Pueyo, L., Carlotti, A., Stark, C. C., , and Perrin, M. D., “Apodized pupil Lyot coronagraphs for arbitrary apertures. v. hybrid shaped pupil designs for imaging Earth-like planets with future space observatories,” *Astrophys. J.* **818**, 163 (2016).
- [2] Zimmerman, N. T., N'Diaye, M., Laurent, K. E. S., Soummer, R., Pueyo, L., Stark, C. C., Sivaramakrishnan, A., Perrin, M., Vanderbei, R. J., Kasdin, N. J., Shaklan, S., and Carlotti, A., “Lyot coronagraph design study for large, segmented space telescope apertures,” *Proc. SPIE* **9904**, 99041Y (2016).
- [3] Ruane, G., Mawet, D., Jewell, J., and Shaklan, S., “Performance and sensitivity of vortex coronagraphs on segmented space telescopes,” *Proc. SPIE* **10400**, 104000J (2017).
- [4] Shaklan, S., “Segmented coronagraph design and analysis (SCDA): A study by the exoplanet exploration program.” <https://exoplanets.nasa.gov/exep/technology/TDEM-awards/> (2017).
- [5] Shi, F., Cady, E., Seo, B.-J., An, X., Balasubramanian, K., Kern, B., Lam, R., Marx, D., Moody, D., Prada, C. M., Patterson, K., Poberezhskiy, I., Shields, J., Sidick, E., Tang, H., Trauger, J., Truong, T., White, V., Wilson, D., and Zhou, H., “Dynamic testbed demonstration of WFIRST coronagraph low order wavefront sensing and control (LOWFS/C),” *Proc. SPIE* **10400**, 104000D (2017).
- [6] Gonsalves, R. A. and Chidlaw, R., “Wavefront sensing by phase retrieval,” *Proc. SPIE* **0207**, 32–39 (1979).

- [7] Fienup, J. R., “Phase-retrieval algorithms for a complicated optical system,” *Appl. Opt.* **32**(10), 1737–1746 (1993).
- [8] Redding, D. C., Basinger, S. A., Lowman, A. E., Kissil, A., Bely, P. Y., Burg, R., Lyon, R. G., Mosier, G. E., Femiano, M., Wilson, M. E., Schunk, R. G., Craig, L. D., Jacobson, D. N., Rakoczy, J. M., and Hadaway, J. B., “Wavefront sensing and control for a Next-Generation Space Telescope,” *Proc. SPIE* **3356** (1998).
- [9] Dean, B. H., Aronstein, D. L., Smith, J. S., Shiri, R., and Acton, D. S., “Phase retrieval algorithm for JWST flight and testbed telescope,” *Proc. SPIE* **6265**, 626511 (2006).
- [10] Fienup, J. R., Marron, J. C., Schulz, T. J., and Seldin, J. H., “Hubble Space Telescope characterized by using phase retrieval algorithms,” *Appl. Opt.* **32**(10), 1747–1767 (1993).
- [11] Redding, D., Dumont, P., and Yu, J., “Hubble Space Telescope prescription retrieval,” *Appl. Opt.* **32**, 1728–1736 (Apr 1993).
- [12] Acton, D. S., Knight, J. S., Contos, A., Grimaldi, S., Terry, J., Lightsey, P., Barto, A., League, B., Dean, B., Smith, J. S., Bowers, C., Aronstein, D., Feinberg, L., Hayden, W., Comeau, T., Soummer, R., Elliott, E., Perrin, M., and Starr, C. W., “Wavefront sensing and controls for the James Webb Space Telescope,” *Proc. SPIE* **8442**, 84422H (2012).
- [13] Gerchberg, R. W. and Saxton, W. O., “A practical algorithm for the determination of phase from image and diffraction plane pictures,” *Optik* **35**(3), 237–246 (1972).
- [14] Fienup, J. R., “Phase retrieval algorithms: a comparison,” *Appl. Opt.* **21**, 2758–2769 (Aug 1982).
- [15] Nocedal, J. and Wright, S., [*Numerical Optimization*], Springer (2006).
- [16] Jurling, A. S. and Fienup, J. R., “Applications of algorithmic differentiation to phase retrieval algorithms,” *J. Opt. Soc. Am. A* **31**(7), 1348–1359 (2014).
- [17] Bloemhof, E. E. and Wallace, J. K., “Phase contrast techniques for wavefront sensing and calibration in adaptive optics,” *Proc. SPIE* **5169**, 309 (2003).
- [18] Aime, C., Soummer, R., and Dohlen, K., “Phase masks in astronomy: From the Mach-Zehnder interferometer to coronagraphs,” *EAS Pub Series* **12**, 33–44 (2004).
- [19] Wallace, J. K., Rao, S., Jensen-Clem, R. M., and Serabyn, G., “Phase-shifting Zernike interferometer wavefront sensor,” *Proc. SPIE* **8126**, 81260F (2011).
- [20] N’Diaye, M., Dohlen, K., Fusco, T., and Paul, B., “Calibration of quasi-static aberrations in exoplanet direct-imaging instruments with a Zernike phase-mask sensor,” *Astron. Astrophys.* **555**, A94 (2013).
- [21] Zernike, F. and Stratton, F. J. M., “Diffraction theory of the knife-edge test and its improved form, the phase-contrast method,” *Mon Not R Astron Soc* **94**, 377–384 (1934).
- [22] Goodman, J. W., [*Introduction to Fourier Optics, 3rd Ed.*], Roberts and Company (2005).
- [23] Surdej, I., Yaitskova, N., and Gonté, F., “On-sky performance of the Zernike phase contrast sensor for the phasing of segmented telescopes,” *Appl. Opt.* **49**(21), 4052–4062 (2010).
- [24] Vigan, A., Dohlen, K., and Mazzanti, S., “On-sky multiwavelength phasing of segmented telescopes with the Zernike phase contrast sensor,” *Appl. Opt.* **50**(17), 2708–2718 (2011).
- [25] Wallace, J. K., Crawford, S., Loya, F., and Moore, J., “A phase-shifting Zernike wavefront sensor for the Palomar P3K adaptive optics system,” *Proc. SPIE* **8447**, 84472K (2012).
- [26] N’Diaye, M., Vigan, A., Dohlen, K., Sauvage, J.-F., Caillat, A., Costille, A., Girard, J. H. V., Beuzit, J.-L., Fusco, T., Blanchard, P., Le Merrer, J., Le Mignant, D., Madec, F., Moreaux, G., Mouillet, D., Puget, P., and Zins, G., “Calibration of quasi-static aberrations in exoplanet direct-imaging instruments with a Zernike phase-mask sensor - II. concept validation with ZELDA on VLT/SPHERE,” *Astron. Astrophys.* **592**, A79 (2016).
- [27] Jurling, A. S. and Fienup, J. R., “Phase retrieval with unknown sampling factors via the two-dimensional chirp-Z transform,” *J. Opt. Soc. Am. A* **31**, 1904–1911 (Sep 2014).
- [28] Moore, D. B. and Fienup, J. R., “Ptychography for optical metrology with limited translation knowledge,” *Appl. Opt.* **55**, 4596–4610 (2016).
- [29] Thurman, S. T. and Fienup, J. R., “Phase retrieval with signal bias,” *J. Opt. Soc. Am. A* **26**(4), 1008–1014 (2009).
- [30] Stark, C., “Luvoirish guide stars,” (2017). Personal communication to D. Redding by electronic mail.

- [31] Crill, B. P. and Siegler, N., “Space technology for directly imaging and characterizing exo-Earths,” Proc. SPIE **10398**, 103980H (2017).